Uniaxial Pressure Control of Competing Orders in a High Temperature Superconductor

Authors:

H.-H. Kim[1†], S. M. Souliou[2†,‡], M.E. Barber[3], E. Lefrancois[1,2], M. Minola[1], M. Tortora[1], R. Heid[5], N. Nandi[3], R. A. Borzi[3,4], G. Garbarino[2], A. Bosak[2], J. Porras[1], T. Loew[1], M. König[3], P.M. Moll[3], A. P. Mackenzie[3], B. Keimer[1], C. W. Hicks[3], M. Le Tacon[5*]

Affiliations:

[1] Max Planck Institute for Solid State Research, Heisenbergstraße 1, D-70569 Stuttgart, Germany.

[2] European Synchrotron Radiation Facility (ESRF), BP 220, F-38043 Grenoble Cedex, France.

[3] Max Planck Institute for Chemical Physics of Solids, Nöthnitzer Straße 40, 01187 Dresden, Germany.

[4] Instituto de Física de Líquidos y Sistemas Biológicos (IFLYSIB), UNLP-CONICET, La Plata, Argentina and Departamento de Física, Facultad de Ciencias Exactas, Universidad Nacional de La Plata, c.c. 16, suc. 4, 1900 La Plata, Argentina.

[5] Institute for Solid State Physics, Karlsruhe Institute of Technology, Hermann-v.-Helmholtz-Platz 176344 Karlsruhe, Germany.

*Correspondence to: matthieu.letacon@kit.edu.

†These authors contributed equally to the present work.

‡Current address: Institute for Solid State Physics, Karlsruhe Institute of Technology, Hermann-v.-Helmholtz-Platz 176344 Karlsruhe, Germany.

Abstract:

Abstract: Cuprates exhibit antiferromagnetic, charge-density-wave (CDW), and high-temperature superconducting ground states that can be tuned by doping and external magnetic fields. However, disorder generated by these tuning methods complicates the interpretation of such experiments. Here, we report a high-resolution inelastic x-ray scattering study of the high-temperature superconductor $YBa_2Cu_3O_{6.67}$ under uniaxial stress, and show that a three-dimensional long-range-ordered CDW state can be induced by pressure along the a-axis, in the absence of magnetic fields. A pronounced softening of an optical phonon mode is associated with the CDW transition. The amplitude of the CDW is suppressed below the superconducting transition temperature, indicating competition with superconductivity. The results provide insights into the normal-state properties of cuprates and illustrate the potential of uniaxial-pressure control of competing orders in quantum materials.

Main Text:

Moderately doped high-temperature superconductors show a ubiquitous tendency towards charge order (1). Manifestations of charge ordering include striped order in lanthanum-based cuprates (2, 3) – an incommensurate modulation of both charge and spin that suppresses superconductivity – and a biaxial charge density wave (CDW) with quasi-two-dimensional (2D) short-range order in the CuO_2 planes of all other cuprate families (*4-12*). The origin of CDW order and its relationship with superconductivity are widely debated issues. It is well-established that static CDW order and superconductivity compete, however it is not clear whether the two orders are best described as mutually incompatible (*7, 8*), as different manifestations of the same pairing interaction (*13*), or as different aspects of a composite order parameter (*14, 15*). These issues have direct and important implications for the mechanism of high-temperature superconductivity (HTSC).

The $YBa_2Cu_3O_{6+x}$ ($YBCO_{6+x}$) family has been particularly well studied because doping-induced structural disorder is less severe than in other families. In this compound, the competition between superconductivity and CDW order is evidenced by the depression of the CDW amplitude upon cooling below the superconducting transition temperature, T_c, *(7,8)* and by its enhancement in magnetic fields that weaken superconductivity (*8,9*). Nuclear Magnetic Resonance (NMR) and x-ray studies further showed that in fields larger than ~15 T a 3D long-range ordered uniaxial CDW (*16-19*) is induced. This 3D order is distinct from the 2D one, although they coexist and are related to each other; for instance, they have the same in-plane incommensurability. The 3D order has an identifiable thermodynamic transition (*20-22*), whereas the 2D CDW onsets gradually (*23-24*), and it is not clear whether it constitutes an alternative ground state, or is, for example, a vestige of the 3D order that is weakened by the interaction with superconductivity.

Here we use inelastic x-ray scattering (IXS) on a sample of $YBCO_{6.67}$ ($T_c = 65$K, doping p = 0.12) to show that uniaxial pressure along the crystallographic a axis can induce long-range 3D CDW order, in the absence of a magnetic field.

We first specify why we chose to work with uniaxial pressures. In the doping range of interest ($0.08 < p < 0.15$), hydrostatic pressure yields, through self-doping and other effects, an increase of T_c (25). A recent study of the biaxial charge modulation further revealed its rapid suppression under hydrostatic pressure (26). However, it has long been established that, at least in the limit of low pressures, the effect of hydrostatic pressure on T_c reflects a net sum of larger effects of uniaxial pressures that almost cancel each other out (27,28). In particular, close to $p \sim 0.12$ where the charge modulation is maximized, uniaxial pressure applied along the a-axis suppresses T_c (ref. 29 and 30)

In this study, we pressurized the sample using a piezoelectric-based apparatus similar to that used in recent studies of ruthenium oxides (31-33), but modified to allow x-ray transmission through the apparatus and the sample. For maximum scattering intensity, the thickness of the sample should match the absorption length at the working wavelength [$\lambda = 0.6968$ Å for this experiment], which is ~ 40 μm. However, to withstand strong compression without buckling, the length-to-thickness ratio of the sample cannot be too large (31), and a 40 μm thickness implies a length that is inconveniently short for reliable mounting. Therefore, we prepared a thicker needle from a $YBCO_{6.67}$ single crystal, then used a plasma focused ion beam to thin down to 40 μm thickness the central portion over ~ 200 μm (Fig. 1). The x-ray beam, with a spot of $50 \times 40 \mu m^2$, was considerably smaller than the thinned central portion of the sample, so highly uniform strain is expected in the probed volume. All the strain values in this paper are calculated using the capacitance sensor, the changes in the c-axis lattice parameter measured from the (0 0 6) Bragg

peak and the changes in T_c (30). The highest compression we reached was $\varepsilon_{xx} \sim -1.0\%$, where ac susceptibility measurements showed that T_c decreases (at a rate increasing with strain) to 48±5 K (30).

The data on the 2D biaxial CDW are shown in Fig. 2. The scattering intensity of the biaxial CDW peaks at the reduced momentum transfer $\boldsymbol{q}_{2D} = (h,k,l) = (0,0.31,0.5)$, in reciprocal lattice units (r.l.u.) of the orthorhombic crystal structure (7, 8). The 3D CDW peaks, in contrast, at $\boldsymbol{q}_{3D} = (0,0.31,1)$ (16-19). In the rest of the paper, we will mostly refer to the total momentum transfers $\boldsymbol{Q}_{2D} = (H,K,L) = (0,0.31,6.5)$ and $\boldsymbol{Q}_{3D} = (0,0.31,7)$ around which measurements were carried out, and where the structure factor of the CDWs is maximum (34,35). The color maps in Figs. 2, A-B show the raw IXS intensity at $\varepsilon_{xx} = 0\%$ (Fig. 2A) and at -1.0% (Fig. 2B). Both data sets were measured below T_c (30). Two characteristic features of the CDW are clearly visible: the quasi-elastic 'central' peak at $\boldsymbol{Q}_{2D}$ and the superconductivity-induced Kohn anomaly in the phonon spectra. In unstrained conditions, the latter consists of a ~15% softening of the low lying acoustical phonon (at ~8 meV) at $\boldsymbol{Q}_{2D}$ (35). Comparing the two panels, it can be seen that the quasi-elastic peak is enhanced by the applied pressure. In Fig. 2C, it is seen that this enhancement occurs smoothly. At the highest strain, the integrated intensity of the peak is a little over two times larger than that of the unstrained sample (Fig. 2D). Its half-width-at-half-maximum (HWHM) σ, which is inversely proportional to the modulation correlation length $\xi = \frac{1}{2\pi\sigma}$, decreases modestly under pressure (Fig. 2D). We did not resolve any shift of $\boldsymbol{Q}_{2D}$ with ε_{xx}. Finally, a comparison of Figs. 2, A and B reveals an increase of the low energy spectral weight under pressure. Its phenomenology and relation to the Kohn anomaly will be discussed below.

We observe a much more notable response to uniaxial pressure in the scattering pattern at $\boldsymbol{Q}_{3D}$. We first look at the strain dependence of the elastic peak intensity along the $\boldsymbol{Q} = (0, 0.315, L)$

line at T = 50 K (Fig. 3A). At $\varepsilon_{xx} = -0.8\%$, a small, narrow peak appears at $\boldsymbol{Q}_{3D}$. When the compression is further increased, to $\varepsilon_{xx} = -1.0\%$, this peak becomes much more intense. It appears on top of the broad profile centered around $l = 0.5$ ($L = 6.5$) that arises from the 2D CDW. The profile of the 3D peak along K is shown on Fig. 3B. A weak 3D peak is visible at compressions as low as $\varepsilon_{xx} = -0.5\%$, however the increase in intensity from 0.8 to 1.0% compression dwarfs the evolution at lower compressions. The evolution of the integrated intensity, and the HWHM along K, are shown in Fig. 3C. At $\varepsilon_{xx} = -1.0\%$, the HWHM is $\sigma_b \sim 0.002$ r.l.u. It is resolution-limited along L ($\sigma_c \sim 0.02$ r.l.u). These correspond to respective (lower bounds for the) correlation lengths of $\xi_b = \frac{1}{2\pi\sigma_b} \sim 80b \sim 310$Å and $\xi_c = \frac{1}{2\pi\sigma_c} \sim 8c \sim 94$Å (the limitations of the scattering geometry did not permit investigation of ξ_a). These correlation lengths are larger than the values reported under a field of 26 T. The correlation lengths of the 2D CDW at 1.0% compression are $\xi_b{}^{2D} \sim 16b \sim 65$Å and $\xi_c{}^{2D} \sim c \sim 12$Å. To estimate the correlation volume $\Xi = \xi_a \times \xi_b \times \xi_c$, we estimate $\xi_a \sim \xi_b$ for both the 2D and 3D CDWs. For the 3D order we find $\Xi \sim 51000$ unit cells under uniaxial pressure for $T \sim T_c$, exceeding by more than two orders of magnitude that of the 2D CDW at ambient conditions ($\Xi \sim 250$ unit cells).

The temperature evolution of the 3D CDW at $\varepsilon_{xx} = -1.0\%$ is shown in Fig. 3, D-F. The peak is very strong at 60 K, and is weaker but still visible at 70 K. That is higher than the onset temperature of the 3D order observed under high field, and higher than the T_c of the unstressed sample. On the low-temperature side, strong competition with superconductivity is apparent. At T=41 K (i.e. below T_c), the peak at $\boldsymbol{Q}_{3D}$ has already lost ~90% of the integrated intensity recorded at 50K and can hardly be distinguished from the background of the 2D order at lower temperatures. This is a much more rapid suppression than that seen for the 2D CDW (7).

To gain further insights on the relationship between the 2D and 3D orders, we investigate the pressure and temperature dependence of the phonon modes in the inelastic part of the spectra. In Fig. 4A, we show the phonon spectra in the absence of applied pressure at T=50 K, along the (0, K, 7) direction. Well away from $\boldsymbol{Q}_{3D}$, three peaks are visible. These are well reproduced in ab initio lattice dynamics calculations (30), and correspond respectively to an acoustic phonon mode of the Δ'_4 irreducible representation (36) at ~8 meV, two optical modes (Δ'_1 and Δ'_4) at ~11 meV (which are not resolvable in the measurement), and another Δ'_1 optical mode at ~15 meV. It can be seen that, in the absence of strain, the acoustic mode softening associated with the 2D CDW (34), and shown at $\boldsymbol{Q}_{2D}$ in Fig. 2A, extends along L and is visible at $\boldsymbol{Q}_{3D}$.

In Fig. 4B, we show the same spectra but with $\varepsilon_{xx} = -1.0\%$ and $T = 41$ K (to stay below T_c). Away from $\boldsymbol{Q}_{3D}$, the spectra are essentially unchanged. Near $\boldsymbol{Q}_{3D}$, on the other hand, a very strong phonon softening is observed, albeit not of the acoustic mode, which now disperses exactly as predicted by the ab initio calculations as K is swept through $\boldsymbol{Q}_{3D}$. In other words, the Kohn anomaly seen in Fig. 4A, at T=50 K and $\varepsilon_{xx} = 0\%$, is no longer present under $\varepsilon_{xx} = -1.0\%$. This suppression of the acoustical Kohn anomaly can also be seen in Fig. 4C, where we show the L-dependence of the phonon spectra from $\boldsymbol{Q}_{2D}$ to $\boldsymbol{Q}_{3D}$ for both $\varepsilon_{xx} = 0$ and $\varepsilon_{xx} = -1.0\%$. Without pressure, the acoustical phonon is soft along the entire L-line, in agreement with the data in Fig. 4A. At $\varepsilon_{xx} = -1.0\%$, we can follow the hardening of the acoustical mode, $i.e.$ the disappearance of the Kohn anomaly, as we traverse from $\boldsymbol{Q}_{2D}$ to $\boldsymbol{Q}_{3D}$. The mode that softens approaching $\boldsymbol{Q}_{3D}$ is a distinct feature, which we therefore identify as one of the optical modes. Figures 4, D and E show the temperature dependence of the phonon modes at $\boldsymbol{Q}_{3D}$. At 70 K the optical phonon is already very soft, which indicates that, unlike the acoustical Kohn anomaly, the optical mode softening is not induced by superconductivity. At 50 and 60K, the soft phonon mode cannot be resolved from the elastic peak (30). In analogy with soft-mode-driven CDW order (e.g. in 2H-

NbSe$_2$ (37)), this suggests a complete softening of this mode. The mode hardens again below 50K, as the long-range CDW order disappears in the superconducting state.

The unambiguous identification of the soft phonon among the 36 allowed optical modes (38) is not a trivial task. Interestingly, both Δ'_1 and Δ'_4 representations include an oxygen bond-stretching phonon around 60 meV (39) that exhibits pronounced dispersion anomalies close to $\boldsymbol{Q}_{3D}$ (40). The buckling mode (Δ'_1) also softens anisotropically along the 010 direction upon entering the superconducting state (41). Various scenarios have been discussed, attributing these anomalies to e.g. coupling of the phonons to dispersive collective charge excitations (42, 43) or to hybridization with lower energy branches of the same symmetry (44).

Further work is required to determine which of these optical modes is driven soft under uniaxial pressure, whether the softening is complete (a continuous hardening of the soft-phonon upon cooling through T_c at $\boldsymbol{Q}_{3D}$ cannot be completely ruled-out with the data at hand – see Fig. 4E) and to understand the mechanism yielding the disappearance of the acoustical phonon Kohn anomaly at $\boldsymbol{Q}_{3D}$. The absence of phonon softening in single-electron calculations indicates that electronic correlations need to be included in any theoretical treatment of the phonon softening and CDW formation (45).

From a theoretical point of view, unidirectional CDW are unstable against disorder, and a vestigial nematic state is expected instead. It has previously been discussed how short-range biaxial modulation of the charge density might emerge from an intrinsic unidirectional CDW instability in presence of quenched disorder (23, 46, 47), which locally reorients small uniaxial domains. Inhomogeneous distribution of the disorder strength has been invoked (18) to explain the appearance of long range unidirectional 3D order alongside with an increase of the 2D order under large magnetic fields. In this model, although one might expect the 3D order to grow at the expense

of the 2D one, this process occurs on top of a general strengthening of CDW order as superconductivity is suppressed by the magnetic field, and inhomogeneity in the strength of disorder allows spatially-separated, coexisting domains of 2D and 3D order.

Similarly, our data indicate that strain tuning efficiently strengthens the CDW and supports the formation of the 3D order, likely primarily in those regions where the pinning strength is the weakest. It will be interesting to see in the future whether the strength of the 2D order does eventually decrease as strain is further increased. More generally, further theoretical work is required to understand the strain-induced strengthening of the CDW, which cannot be solely attributed to the competition with superconductivity because the 3D CDW peak can already be induced above the nominal T_c of the sample.

We conclude by noting that uniaxial stress will allow the relationship between the superconductivity and CDW to be investigated with high precision in future experiments. A magnetic field suppresses type-II superconductivity inhomogeneously, thanks to the presence of vortices, resulting in broad transitions. In contrast, the homogeneous tuning provided by stress could for instance allow to determine using thermodynamic probes whether the CDW and superconductivity can coexist microscopically. Our piezoelectric-based apparatus constitutes a versatile tool that can be implemented in a large variety of experimental setups, in particular at synchrotron facilities, thus opening perspectives for the study of correlated-electron materials.

References and Notes:

1. B. Keimer, S. A. Kivelson, M. R. Norman, S. Uchida, J. Zaanen, *Nature* **518**, 179-186 (2015).

2. J. M. Tranquada, B. J. Sternlieb, J. D. Axe, Y. Nakamura, S. Uchida, *Nature* **375**, 561-563 (1995).

3. M. Vojta, *Advances in Physics* **58**, 699-820 (2009).

4. J. E. Hoffman *et al.*, *Science* **295**, 466 (2002).

5. C. Howald, H. Eisaki, N. Kaneko, M. Greven, A. Kapitulnik, *Phys. Rev. B* **67**, 014533 (2003).

6. W. D. Wise *et al.*, *Nature Physics* **4**, 696-699 (2008).

7. G. Ghiringhelli *et al.*, *Science* **337**, 821-825 (2012).

8. J. Chang *et al.*, *Nature Physics* **8**, 871-876 (2012).

9. S. Blanco-Canosa *et al.*, *Phys. Rev. Lett.* **110**, 187001 (2013).

10. T. P. Croft, C. Lester, M. S. Senn, A. Bombardi, S. M. Hayden, *Phys. Rev. B* **89**, 224513 (2014).

11. E. H. da Silva Neto *et al.*, *Science Advances* **2**, 1600782 (2016).

12. W. Tabis *et al.*, *Phys. Rev. B* **96**, 134510 (2017).

13. A. Perali, C. Castellani, C. Di Castro, M. Grilli, *Phys. Rev. B* **54**, 16212 (1996).

14. S. A. Kivelson, E. Fradkin, V. J. Emery, *Nature* **393**, 550-553 (1998).

15. L. E. Hayward, D. G. Hawthorn, R. G. Melko, S. Sachdev, *Science* **343**, 1336-1339 (2014).

16. T. Wu *et al.*, *Nature Communications* **6**, (2015).

17. S. Gerber *et al.*, *Science* **350**, 949-952 (2015).

18. H. Jang *et al.*, *Proceedings of the National Academy of Sciences* **113**, 14645-14650 (2016).

19. J. Chang *et al.*, *Nature Communications* **7**, 11494 (2016).

20. F. Yu *et al.*, *Proceedings of the National Academy of Sciences* **113**, 12667-12672 (2016).

21. D. LeBoeuf *et al.*, *Nature Physics* **9**, 79-83 (2013).

22. T. Wu *et al.*, *Nature* **477**, 191-194 (2011).

23. L. Nie, L. E. H. Sierens, R. G. Melko, S. Sachdev, S. A. Kivelson, *Phys. Rev. B* **92**, 174505 (2015).

24. Y. Caplan, G. Wachtel, D. Orgad, *Phys. Rev. B* **92**, 224504 (2015).

25. S. Sadewasser, J. S. Schilling, A. P. Paulikas, B. W. Veal, *Phys. Rev. B* **61**, 741-749 (2000).

26. S. M. Souliou *et al.*, *Phys. Rev. B* **97**, 020503 (2018).

27. C. Meingast *et al.*, *Phys. Rev. Lett.* **67**, 1634 (1991).

28. U. Welp *et al.*, *Phys. Rev. Lett.* **69**, 2130-2133 (1992).

29. O. Kraut *et al.*, *Physica C: Superconductivity* **205**, 139-146 (1993).

30. Materials and methods are available as supplementary materials.

31. C. W. Hicks *et al.*, *Science* **344**, 283-285 (2014).

32. C. W. Hicks, M. E. Barber, S. D. Edkins, D. O. Brodsky, A. P. Mackenzie, *Review of Scientific Instruments* **85**, 065003 (2014).

33. A. Steppke *et al.*, *Science* **355**, 148 (2017).

34. M. Le Tacon *et al.*, *Nature Physics* **10**, 52-58 (2014).

35. E. M. Forgan *et al.*, *Nature Communications* **6**, 10064 (2015).

36. K.-P. Bohnen, R. Heid, M. Krauss, *Europhys Lett* **64**, 104-110 (2003).

37. F. Weber *et al.*, Physical Review Letters **107**, 107403 (2011).

38. In presence of the oxygen-superstructure at this doping level (Ortho-VIII), even more phonons can be expected (36 is the number of optical modes expected for the ortho-I structure of $YBa_2Cu_3O_7$).

39. D. Reznik *et al.*, *Nature* **440**, 1170-1173 (2006).

40. D. Reznik, *Physica C: Superconductivity* **481**, 75-92 (2012).

41. M. Raichle *et al.*, *Phys. Rev. Lett.* **107**, 177004 (2011).

42. L. Chaix *et al.*, *Nature Physics* **13**, 952 (2017).

43. E. Kaneshita, M. Ichioka, K. Machida, *Phys. Rev. Lett.* **88**, 115501 (2002).

44. L. Pintschovius *et al.*, *Phys. Rev. B* **69**, 214506 (2004).

45. Z. P. Yin, A. Kutepov, G. Kotliar, *Phys. Rev. X* **3**, 021011 (2013).

46. J. A. Robertson, S. A. Kivelson, E. Fradkin, A. C. Fang, A. Kapitulnik, *Phys. Rev. B* **74**, 134507 (2006).

47. A. Del Maestro, B. Rosenow, S. Sachdev, *Phys. Rev. B* **74**, 024520 (2006).

48. C. T. Lin, W. Zhou, W. Y. Liang, E. Schönherr, H. Bender, *Physica C: Superconductivity* **195**, 291 (1992).

49. M. Lei, J. L. Sarrao, W. M. Visscher, T. M. Bell, J. D. Thompson, A. Migliori, U. W. Welp, B. W. Veal, *Phys. Rev. B* **47**, 6154 (1993).

50. S. G. Louie, K.-M. Ho, M. L. Cohen, *Phys. Rev. B* **19**, 1774 (1979).

51. C. Elsässer, N. Takeuchi, K.-M. Ho, C. T. Chan, P. Braun, M. Fähnle, *J. Phys.: Condens. Matter* **2**, 4371 (1990).

52. L. Hedin and B. I. Lundqvist, *Journal of Physics C: Solid State Physics* **4**, 2064 (1971).

53. K. P. Bohnen, R. Heid, M. Krauss, *Europhysics Letters* **64**, 104 (2003).

54. R. Heid and K. P. Bohnen, *Physical Review B* **60**, R3709 (1999).

55. E. Burkel, *Report on Progress in Physics* **63**, 171 (2000).

Author contributions: IXS experiments were carried out by S.M.S., H.-H.K., E.L., M.M., M.T., A.B. and M.L.T. IXS data were analyzed by S.M.S. and M.L.T. XRD experiments were carried out by H.-H.K., S.M.S., E.L., M.E.B., M.T., M.M., G.G., C.W.H. and M.L.T. R.H. carried out the ab initio calculations.

M.E.B., N.N., R.A.B., and C.W.H. performed the susceptibility measurements. Single crystals studied in this work were prepared by J.P., T.L. and S.M.S. PFIB preparation was carried out by P.M.M. and M.K. The strain devices used in this study were built by C.W.H. with assistance from M.L.T., H.-H.K., and E.L. S.M.S. and M.L.T. conceived the project. A.P.M., B.K., C.W.H. and M.L.T. supervised the project. M.L.T. and C.W.H. wrote the manuscript with input from all the coauthors.

Competing interests: C.W.H. has 31% ownership of Razorbill Instruments, which has commercialized apparatus on which that used in this work are based.

Data and materials availability: Raw data and simulation codes used for all figures in this paper and the supplementary materials are available at http://dx.doi.org/10.5445/IR/1000086708
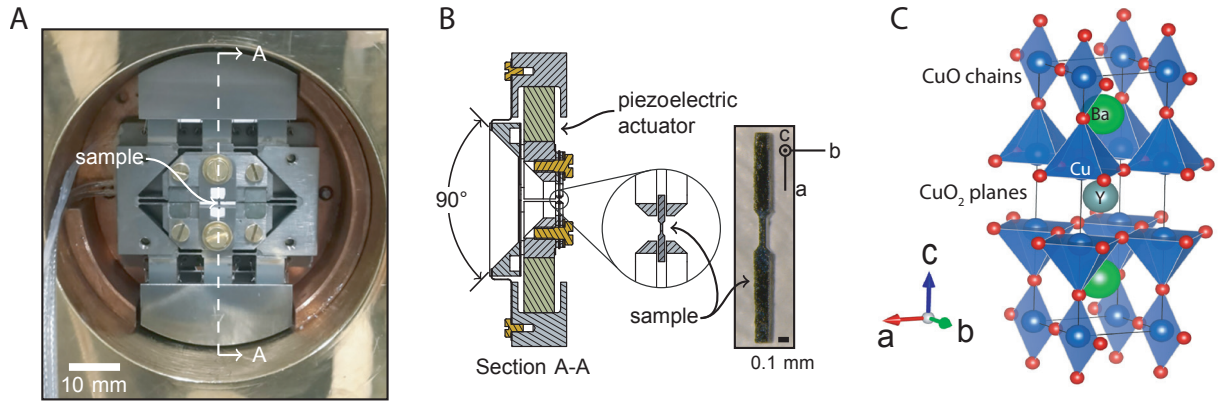
Fig. 1 Strain device (A) Photograph of the Piezo-electric device (B) Sectional cut of the device and picture of the Focused-Ion-Beam-thinned sample used for this experiment. (C) Unit cell of $YBa_2Cu_3O_{6+x}$ (here with x=1). Strain is applied perpendicular to the CuO chains.
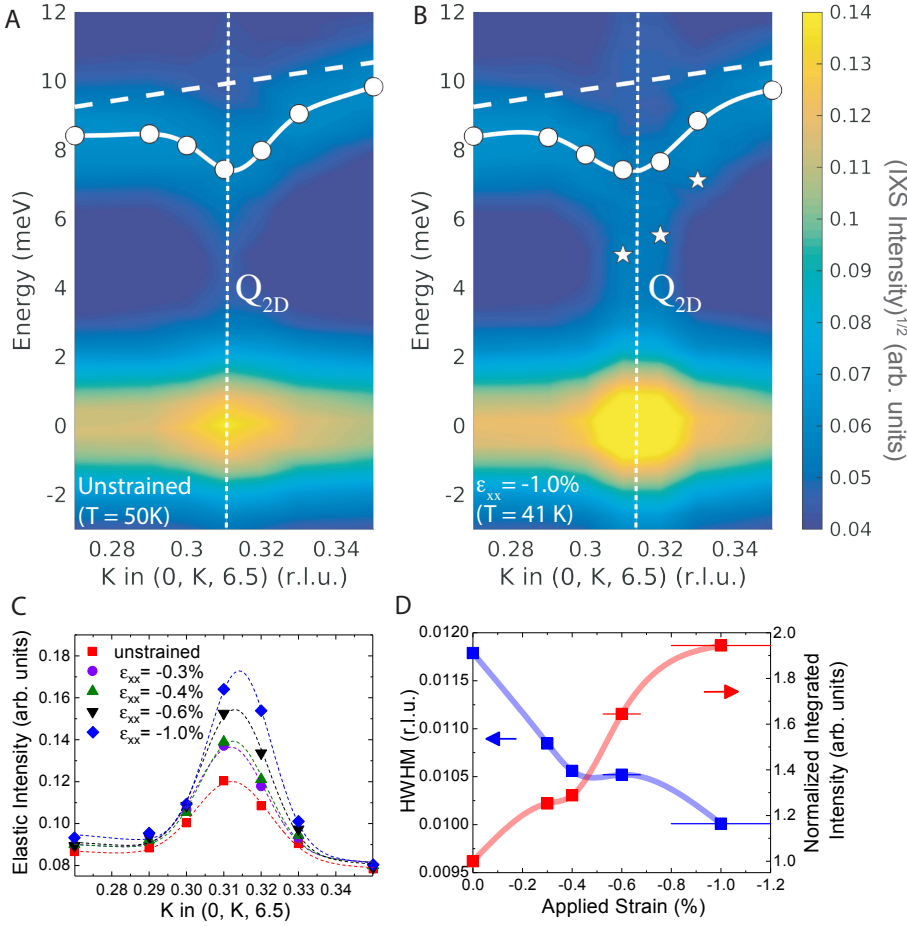
Fig. 2. Strain dependence of the IXS spectra around Q_{2D}. (A) IXS intensity vs total momentum transfer for the unstrained sample at $T < T_c$. Square root of the intensity has been plotted to enhance the contrast between the phonon and the elastic line. The calculated dispersion of the low-lying acoustical mode is plotted as a dashed line. The plain line is a guide to the eye to the observed dispersion of this mode (fitted values are represented by the dots). (B) Same as in (A), but for $\varepsilon_{xx} = -1.0\%$ (the stars indicate the energy of the soft optical phonon). (C) Strain-dependence of the quasi-elastic line intensity across Q_{2D} along the (0, K,6.5) direction. (D) Strain dependence of the half-width-at-half-maximum and of the integrated intensity (normalized to the unstrained value) of the quasi-elastic line at Q_{2D}, integrated along K and normalized to the unstrained value.
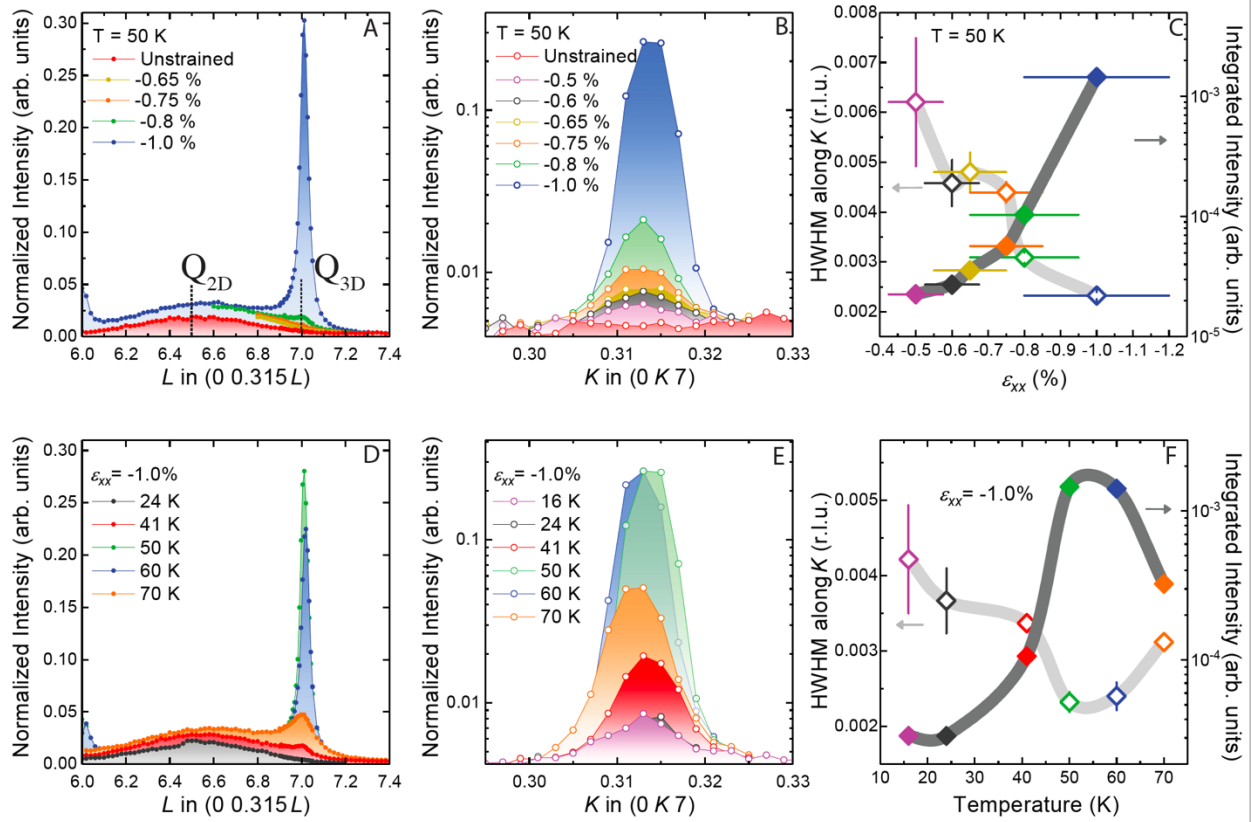
Fig. 3. Strain dependence of the quasi-elastic line at Q_{3D}. (A) Quasi-elastic intensity at T= 50 K along the (0 0.315 L) direction as function of a-axis compression ε_{xx}. (B) Quasi-elastic intensity at T= 50 K along the (0 K 7) direction as function of a-axis compression ε_{xx}. (C) Strain dependence of the HWHM and the integrated intensity along the (0 K 7) direction at T=50 K. (D) Temperature dependence of the quasi-elastic intensity along the (0 0.315 L) direction for $\varepsilon_{xx} = -1.0\%$. (E) Temperature dependence of the quasi-elastic intensity along the (0 K 7) direction for $\varepsilon_{xx} = -1.0\%$. (F) HWHM and integrated intensities vs Temperature at Q_{3D} for $\varepsilon_{xx} = -1.0\%$.
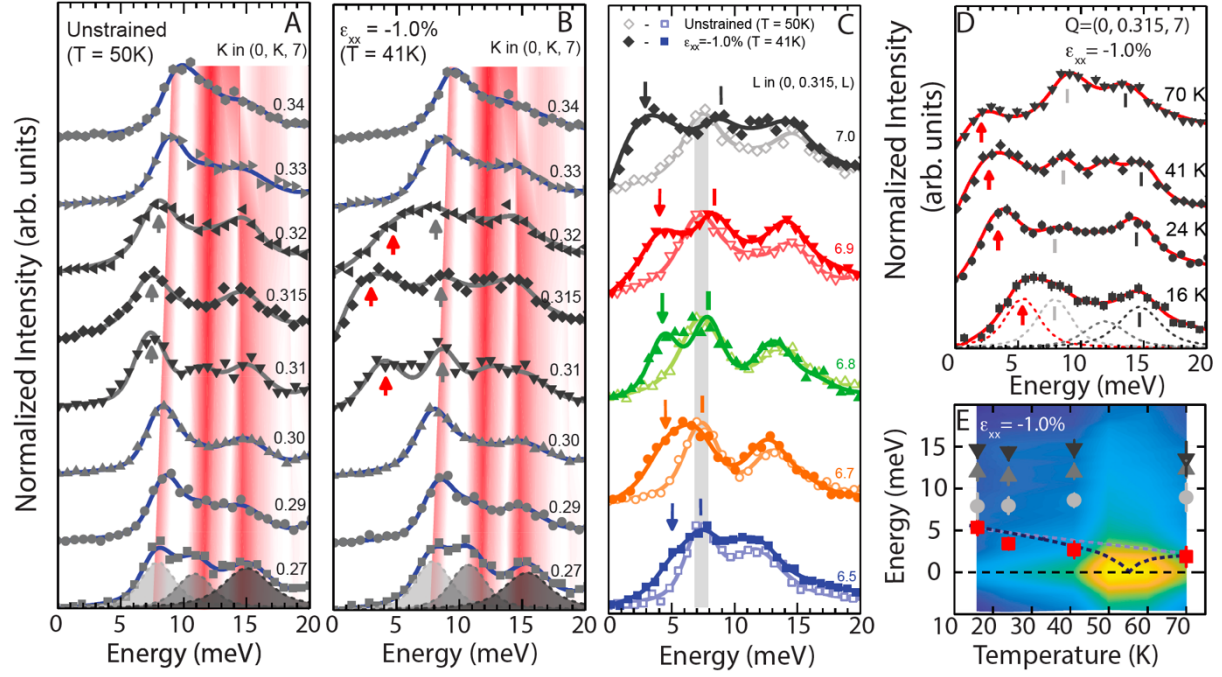
Fig. 4. Strain dependence of the phonon spectra around $\boldsymbol{Q}_{3D}$. (A) Inelastic x-ray scattering intensity (elastic line has been subtracted (30) recorded below T_c along the (0 K 7) direction, in the absence of strain (at T = 50 K) and (B) for $\varepsilon_{xx} = -1.0\%$ (T = 41 K). In both panels, the red lines represent the calculated structure factor of the phonons (30), the gray arrows indicate the acoustical phonon, the red ones the soft optical mode. (C) L-dependence of the inelastic spectra below T_c without (open symbols – T =50 K) and with $\varepsilon_{xx} = -1.0\%$ applied strain (closed symbols– T =41 K). The ticks correspond to the energy of the acoustical mode in the strained case, the arrows to that of the soft optical phonon. (D) Temperature dependence of the phonon spectra at $\boldsymbol{Q}_{3D}$ for $\varepsilon_{xx} = -1.0\%$. Solid lines in panels (A)-(D) correspond to the least square fitting of the data (30) (E) Phonon energy vs temperature superimposed to the IXS intensity color map (log scale) at $\boldsymbol{Q}_{3D}$ for $\varepsilon_{xx} = -1.0\%$. Dotted lines are guide to the eyes for possible scenarios for the temperature dependence of the soft-phonon energy.